Soft Matter

Accepted Manuscript

This is an *Accepted Manuscript*, which has been through the Royal Society of Chemistry peer review process and has been accepted for publication.

Accepted Manuscripts are published online shortly after acceptance, before technical editing, formatting and proof reading. Using this free service, authors can make their results available to the community, in citable form, before we publish the edited article. We will replace this *Accepted Manuscript* with the edited and formatted *Advance Article* as soon as it is available.

You can find more information about *Accepted Manuscripts* in the **Information for Authors**.

Control of the breakup process of viscous droplets by external electric field inside a microfluidic device

Yuehao Li[1], Mranal Jain[1], Yongting Ma[1], Krishnaswamy Nandakumar[1*]

[1]Cain Department of Chemical Engineering, Louisiana State University, Baton Rouge 70802

* Corresponding author email address: nandakumar@lsu.edu

Abstract

Droplet-based microfluidic devices have received extensive attention in the fields of chemical synthesis, biochemical analysis, lab-on-chip devices etc. Conventional passive microfluidic hydrodynamic flow–focusing devices (HFFD) control the droplet breakup process by manipulating the flow ratios of the continuous phase to the dispersed phase. They confront difficulties in controlling droplet sizes in dripping regime especially when the dispersed phase has a large viscosity. Previous studies have reported that external electric field can be utilized as an additional tool to control the droplet breakup process in the microfluidic devices. In this computational fluid dynamics (CFD) study, we have investigated the effect of external static electric field on droplet breakup process using the conservative level–set method coupled with the electrostatic model. The numerical simulations have demonstrated that the interaction of the electric field and the electric charges on the fluid interface induces the electric force, which plays a significant role in controlling the droplet formation dynamics. If the microfluidic system is applied with the electric field of varying strengths, the droplet breakup process experiences three distinct regimes. In Regime 1 where low electric voltages are applied, the droplet size decreases almost linearly with the increase of the voltage. Then the droplet size increases with the applied voltages in Regime 2 where the electric field has moderate strengths. In Regime 3 in which very large voltages are applied, the droplet size decreases with the applied voltage again. These interesting variations in the droplet breakup processes are explained by using transient pressure profiles in dispersed phase and continuous phase. The droplet breakup processes regulated by an external electric field that are revealed in this study can provide useful guidance on the design and operations of such droplet-based systems.

Keywords

Droplet-based microfluidics; hydrodynamic flow–focusing device; static electric field; conservative level–set method; perfect dielectric model

1. Introduction

Droplet–based microfluidics has received special attentions in recent years due to its superior control over fluid flow as well as other unique advantages reported in the literature[1, 2]. By introducing two immiscible fluids into a microfluidic system, the reagent fluid is encapsulated inside discrete droplets or slugs of micro–liter volume[3]. Compared to conventional microfluidic systems using single–phase flow, droplet–based microfluidics provides several unique advantages such as rapid mixing[4-6], reduced dispersion and minimized surface fouling[3]. These advantages have enabled numerous applications of droplet–based microfluidics, such as DNA analysis, protein crystallization, chemical synthesis and other fields[7-9].

For most of these applications, the generation of uniform droplets with desired sizes is the key challenge. Most of current droplet–generating techniques shown in literatures are based on passive methods which utilize device geometry and operations of fluid flow. According to the operations of fluid flow, the passive droplet–generating devices can be generally categorized as co–flow, cross–flow (T–junction) and hydrodynamic flow–focusing[10]. In all of these mentioned devices, the flow rates of the continuous and dispersed phases are manipulated to control the droplet breakup process. By tuning the flow ratios of the two phases (*i.e.*, the flow rate of the continuous phase to the dispersed phase), the relative magnitudes of pressure across the fluid interface, viscous stress and surface stress[11] are altered which in turn results in different breakup patterns. Based on the relative magnitudes of these forces, the breakup patterns can be classified into three distinct regimes. Namely, they are the squeezing, dripping and jetting regimes[10]. Previous studies in literatures have shown that droplets generated by passive methods usually have sizes comparable to the key dimensions of devices[10, 12]. For example, the diameters of droplets produced by hydrodynamic flow–focusing devices (HFFD) usually approximate to

orifice sizes [12]. If the droplets of small sizes are required, the HFFD have to be operated in the dripping regime with very high flow ratios. However, this approach is not effective for many circumstances especially when the dispersed phase is more viscous than the continuous phase. For example, Nie *et al.* have used silicone oil with different viscosities as the dispersed phase and aqueous solutions as the continuous phase to study the droplet breakup process in a HFFD. If the viscosities of the dispersed and continuous phases were 50 cp and 1 cp respectively, the resultant droplets remained large in size for a broad range of operating flow ratios. They concluded that the droplet sizes are marginally affected by increasing flow ratios when the dispersed phase has much larger viscosities than those of the continuous phase[13]. In such circumstances, active droplet–based microfluidic devices can provide more effective control over droplet sizes compared to passive devices. The active techniques utilize external actuators, such as deflected membranes[14], pressure chambers[15], acoustic waves[16, 17] and electric fields[18-21] to provide external forces during droplet breakup processes. By introducing external static electric field to conventional microfluidic devices, Link *et al.* have developed modules that were able to precisely control the droplet motions involving breakup, coalescence, sorting, and *etc*[19].

The concept of employing external electric field to control the droplet breakup in microfluidic devices is similar to that of the electrospray or electro–hydrodynamic atomization (EDHA) technique, which has been used for the fabrication of mono–dispersed polymeric particles[22, 23]. In EDHA, the droplet breakup process is primarily controlled by the strengths of electric field and the flow rates of the dispersed phase while the continuous phase usually remains static. In microfluidic devices incorporated with external electric field, an additional parameter that is the flow rate of the continuous phase can be manipulated to control the droplet breakup process as well. For such systems, conventional microfluidic devices, *i.e.*, microfluidic HFFDs, are embedded with electrodes that are attached to direct current (DC) or alternative current (AC) power supplies. Due to the differences of the electrical properties existing between the continuous and dispersed phases, *i.e.*, the electric permittivity and conductivity, surface charges including

polarization charges and free charges are induced by the electric field. The interaction of the electric field and the surface charges results in an additional electrical force on the fluid interface, which is known as Maxwell stress. With appropriate distributions of the electric field in the microfluidic devices, Maxwell stress provides an additional handle to break droplets from the disperse phase. Hence the droplet sizes can be controlled by both operating flow ratios and electric field strengths. Link *et al*[19]. have studied the effect of the electric field strength on droplet sizes in a microfluidic HFFD coupled with DC electric field. They have shown that droplet sizes decreased remarkably when the applied voltages exceeded a threshold value. Kim *et al.* have also explored the dependence of droplet sizes on DC field strengths, and they reported similar results as those from Link *et al*. In addition, they demonstrated that tiny water–in–oil droplets, which were much less than the orifice width, could be generated in a microfluidic HFFD with the aid of very strong electric field[24].

Despite those experimental explorations, the fundamentals of how external electric field influences the droplet breakup process in the microfluidic devices have not been fully understood yet. Since many parameters are playing roles, *i.e.*, the flow rates of both continuous and dispersed phases, the fluid properties, the electrical properties and *etc.*, the dynamics of the breakup process has remained complicated to study. Numerical simulations have provided an effective way to obtain the insightful information about the breakup process. Herein, we present our work of using computational fluid dynamic (CFD) simulations to study the effect of external DC electric field on controlling the breakup of viscous oil droplets inside a conventional microfluidic HFFD. There are two objectives for this study: (1) to understand why conventional microfluidic HFFDs are ineffective to control the droplet sizes when the viscosity of the dispersed phase is much larger than that of the continuous phase; (2) to investigate how the electric force interacts with the hydrodynamic forces to influence the droplet breakup processes. The dispersed phase used by this study was silicone oil with large viscosities, and the continuous phase was an aqueous solution that is much less viscous compared to the dispersed phase. In Section 2, we present our numerical

4

model that couples the conservative level–set method (LSM) with the electrostatic model. In Section 3.1, the droplet breakup processes in the absent of electric field are investigated. The simulation results indicate that the viscous lubrication effect undermines the ability of conventional microfluidic HFFDs in controlling the droplet sizes, consequently leading to constant droplet sizes in a wide range of operating flow ratios. In Section 3.2, a conventional microfluidic HFFD is incorporated with external electric field, and the droplet breakup processes controlled by electric field of varying strengths are investigated. Three distinct regimes resulting from the interactions between the hydrodynamic forces and the electric forces are demonstrated subsequently. The resultant droplet sizes are reduced noticeably when the electric field with moderate strengths are applied to the system. From a practical point of view, our study may benefit the understanding of the droplet breakup process and provide guidelines to the designs and operations of droplet–based microfluidic devices.

2. Numerical Methods

In this section, we present our model which combines the conservative level–set method (LSM) with the electrostatic model. In such model, the motions of the fluid interface between the two phases are tracked by the conservative level–set method (LSM). A body force term describing the electric stress is added to the Navier–Stokes equations in order to take account of the effect of the electric field on the droplet breakup dynamics. The distributions of the electric field are estimated by the electro static equation simplified with the perfect dielectric assumption. All the equations in this section are presented in the dimensionless forms. The superscript * denotes dimensionless quantities. The subscript d and c refer to dispersed and continuous phases, respectively.

2.1 Governing equations for electric field

The distributions of electric field are governed by the normalized Poisson's equation:

$$\nabla \cdot (\varepsilon^* \nabla V^*) = \rho_f^* \tag{1}$$

where ε^* is the permittivity of the medium; V^* is the electric potential; and ρ_f^* is the volumetric free charge density. The normalized electric field $\boldsymbol{E}^*$ is related to the electric potential through the equation:

$$\boldsymbol{E}^* = -\nabla V^* \tag{2}$$

Since the electric permittivity values of the two phases are different in this study, ε^* varies across the fluid interface. Consequently, the electric field changes not only in its strength but also in its direction as it crosses the fluid interface. The permittivity value is weighted according to the level–set function ϕ by Eq. (3):

$$\varepsilon^* = 1 + (\varepsilon_d/\varepsilon_c - 1)\phi \tag{3}$$

in which ε_c and ε_d are the permittivity values of the continuous and dispersed phases, respectively; ϕ is the level–set function. In this study, ε^*, V^*, ρ_f^* and E^* are scaled with respect to the characteristic quantities such as ε_c, V_0, $\varepsilon_c V_0/w_o^2$ and V_0/l_e, respectively, of which V_0 is the applied voltage on the left side inlet, w_o is the width of orifice and l_e is the distance between the left and right side inlets.

2.2 Governing equations for the fluid flow

In this study, the interface between the two phases is tracked by the conservative level–set method (LSM). The conventional LSM was initially introduced by Osher and Sethain in 1988[25] and was further developed by Sussman, Smereka, and Osher in 1994[26]. It has now emerged as a popular method to simulate the multiphase flow problems. Besides being robust, LSM does not adopt geometric constructions thus can represent the interfacial variables such as the interfacial normal and curvature accurately. As the level–set function ϕ transits across the interface smoothly, the standard discretization of the interfacial variables by using ϕ can achieve high order accuracy, *i.e.*, the secondary–order or higher accuracy. These advantages are especially beneficial to this study: as a thin filament is formed inside the orifice, accurate predictions of the surface normal and curvature are critical to estimate the surface tension force,

electric body force and other quantities. One drawback associated with conventional LSM is the

large computational cost compared to other methods such as the volume of fluid (VOF) method.

The other drawback is the non–conservation of mass, which has also been found in our

preliminary study as well. To overcome such drawback, the conservative form of LSM was

adopted in this study.

Since 2005, Olsson and Kresis have proposed a conservative form of LSM, and this

method has been demonstrated to be able to solve the mass conservation issue successfully[27]. By

using the conservative form, the exact numerical conservation of the integral of ϕ can be obtained.

The conservative form is expressed as

$$\frac{\partial}{\partial t^*}\phi + \nabla \cdot (\boldsymbol{u}^*\phi) = \gamma_{ls}^*\nabla \cdot \left(\epsilon_{ls}^*\nabla\phi - \phi(1-\phi)\frac{\nabla\phi}{|\nabla\phi|}\right) \tag{4}$$

where the level–set function ϕ is a smooth function ranging between 0 and 1; $\boldsymbol{u}^*$ is the velocity

field predicted by the Navier–Stokes equations. If $\phi = 0$, it corresponds to the continuous phase;

if $\phi = 1$, it stands for the dispersed phase. Across the fluid interface, ϕ transits smoothly from 0

to 1. The left–hand side of Eq. (4) is an advection equation of ϕ throughout the computational

domain; since it is unstable in terms of computation, the terms on the right–hand side are added to

enhance the computational stability. The normalized level–set parameter $\epsilon_{ls}^* = \epsilon_{ls}/w_o$ determines

the thickness of the interface where ϕ goes smoothly from 0 to 1. The dimensional parameter ϵ_{ls}

(unit: m) has the same order as the computational mesh size of those elements which the fluid

interface propagates through; it was specified as 5 μm in this study. The normalized re-

initialization parameter $\gamma_{ls}^* = \gamma_{ls}/u_c$ determines the amount of reinitialization or stabilization of

the level–set function. Here u_c refers to the average velocity of the continuous phase in the orifice

region, which is calculated by dividing the flow rate of the continuous phase with the cross–

sectional area of the orifice. In this study, the dimensional parameter γ_{ls} (unit: m/s) was specified

with a value close to u_c. The dimensionless time, t^*, was scaled with respect to the characteristic

time scale w_o/u_c.

The normalized interfacial variables such as the unit normal of fluid interface $\hat{\boldsymbol{n}}$ and the curvature κ^* are calculated based on ϕ as seen in Eq. (5) and Eq. (6):

$$\hat{\boldsymbol{n}} = \nabla\phi/|\nabla\phi| \tag{5}$$

$$\kappa^* = -\nabla \cdot \hat{\boldsymbol{n}}|_{\phi=0.5} \tag{6}$$

The normalized interfacial tension force acting on the interface is then estimated by

$$\boldsymbol{F}_{sf}^* = We_c^{-1}\kappa^*\delta\hat{\boldsymbol{n}} \tag{7}$$

in which the Weber number ($We_c = \rho_c u_c^2 w_o/\sigma$) represents the ratio of inertial forces to interfacial forces; σ is the interfacial tension coefficient (unit: N/m); δ is a Dirac delta function indicating the location of the interface, which is approximated by a smooth function shown in Eq. (8):

$$\delta = 6|\nabla\phi||\phi(1-\phi)| \tag{8}$$

The conservative LSM solves one–set of the Navier–Stokes equations with the assumption that both phases are Newtonian and incompressible. The normalized fluid properties used by the Navier–Stokes equations are weighted by ϕ across the interface:

$$\rho^* = 1 + (\rho_d/\rho_c - 1)\phi \tag{9}$$

$$\mu^* = 1 + (\mu_d/\mu_c - 1)\phi \tag{10}$$

in which ρ_c and ρ_d are the densities of the continuous phase and the dispersed phase; μ_c and μ_d are the viscosities of the two phases, respectively. Although the density and viscosity in each of the bulk phases is a constant, their variations across the fluid interface are determined by ϕ. Considering that ρ^* are functions of time and spatial variables as ϕ propagates, the continuity equation for the entire computational domain is described by:

$$\frac{\partial}{\partial t^*}\rho^* + \nabla \cdot (\rho^*\boldsymbol{u}^*) = 0 \tag{11}$$

The normalized momentum equations are given by:

$$\frac{\partial}{\partial t^*}(\rho^*\boldsymbol{u}^*) + \nabla \cdot (\rho^*\boldsymbol{u}^*\boldsymbol{u}^*) = -\nabla p^* + Re_c^{-1}\nabla \cdot [\mu^*(\nabla\boldsymbol{u}^* + (\nabla\boldsymbol{u}^*)^T)] + \boldsymbol{F}_{sf}^* + \boldsymbol{F}_{ef}^* \tag{12}$$

where the Reynolds number ($Re_c = \rho_c u_c w_o / \mu_c$) represents the ratio of inertial forces to the viscosity forces; p^* is the dimensionless pressure, which is scaled with respect to $\rho_c u_c^2$; $\boldsymbol{F}_{sf}^*$ is the dimensionless surface tension force formulated by Eq.(7); $\boldsymbol{F}_{ef}^*$ is the dimensionless electric force which is shown in the following section. As the density difference between the two phases is small, the buoyance effect was neglected in this study.

The electric body force $\boldsymbol{F}_{ef}^*$ is computed by taking the divergence of Maxwell stress tensor ($\boldsymbol{T}_{MW}^*$) with the assumption of incompressible fluid[28-30]:

$$\boldsymbol{F}_{ef}^* = Eu^{-1}\nabla \cdot \boldsymbol{T}_{MW}^* = -\frac{1}{2}Eu^{-1}(\boldsymbol{E}^* \cdot \boldsymbol{E}^*)\nabla\varepsilon^* + Eu^{-1}\rho_f^*\boldsymbol{E}^* \tag{13}$$

in which the electric Euler number ($Eu = \rho_c u_c^2 / E_0^2 \varepsilon_0 \varepsilon_c$) represents the ratio of inertial forces to electric forces. The first term of Eq. (13), $-\frac{1}{2}Eu^{-1}(\boldsymbol{E}^* \cdot \boldsymbol{E}^*)\nabla\varepsilon^*$, estimates the component of the electric force contributed by the polarization charges. Such charges are induced by the varying electric permittivity across the interface. The direction of this force component is determined by $\nabla\varepsilon^*$. The second term $Eu^{-1}\rho_f^*\boldsymbol{E}^*$ takes account of the contribution by the interaction between free charges and the electric field. The direction of this force component is same as that of the electric field.

2.3 Perfect dielectric model

In order to estimate the free charge density ρ_f^* on the fluid interface, the transport equations of the ionic species have to be taken into account. Although the governing equations that describe the transport of the free electric charges inside electric field have been reported in literatures[28, 30], there still remain difficulties in solving these equations. The key issue is related to the definition of the electrostatic boundary condition on the fluid interface[29]. The relationship of the individual ionic species concentrations between the two phases is still not clear, which requires detailed chemistry of the system to invoke[29, 31]. Currently in literatures, the transport equations of the ionic species are usually simplified by making suitable assumptions. Three

simplified models have been reported: they are the perfect conductor model[32], the perfect

dielectric model[33, 34] and the leaky dielectric model[35, 36], respectively.

In this study, the perfect dielectric model is adopted based on the assumption that the

fluids in the continuous and dispersed phases can be regarded as dielectric materials. Therefore,

the concentration of the free charges on the interface is negligible compared to that of the

polarization charges. The governing equation of the electrostatics shown in Eq. (1) is then

simplified to the Laplace equation:

$$\nabla \cdot (\varepsilon^* \nabla V^*) = 0 \tag{14}$$

Accordingly, the electric body force F_{ef}^* shown in Eq. (13) contains the component

contributed by the polarization charges only:

$$F_{ef}^* = -\frac{1}{2} E u^{-1} (E^* \cdot E^*) \nabla \varepsilon^* \tag{15}$$

As there is no accumulation of the free charges on the fluid interface, the corresponding

boundary conditions on the fluid interface for Eq. (14) are:

$$V_c^* = V_d^* \tag{16}$$

$$E_c^* \cdot \hat{n}_c + (\varepsilon_d / \varepsilon_c) E_d^* \cdot \hat{n}_d = 0 \tag{17}$$

in which V_c^* and V_d^* stand for the electric potential measured from the sides of the continuous

phase and dispersed phase, respectively; E_c^* and E_d^* represents the electric field on the sides of the

respective two phases; $\hat{n}_c$ and $\hat{n}_d$ are the unit normal of the fluid interface measured from the

sides of the respective two phases. The Eq. (16) and (17) represents the continuities of the electric

potential and displacement on the fluid interface.

2.4 Simulation setup

In this study, the geometry of the microfluidic device, the fluid properties and the

operating flow rates followed those have been reported by Nie *et al.* in 2008[13]. A conventional

microfluidic hydrodynamic flow–focusing device (HFFD) was selected to generate droplets. The

dimensions of the geometry are shown in Figure 1. The width of the orifice w_o is 80 μm, and the

microfluidic channels have uniform depth as 86 μm. The continuous phase, which is an aqueous solution with the density and viscosity close to water, is injected from two side inlets with identical flow rates as ½ Q_c. The dispersed phase, which is silicone oil with much larger viscosity compared to that of continuous phase, is injected from the center channel with a flow rate as Q_d. In the flow–focusing chamber, the dispersed phase is focused by the two streams of continuous phase. These three streams flow concurrently through an orifice of confined spaces while the continuous phase continues to squeeze the dispersed phase. After they are pinched off from the dispersed phase, droplets travel through the expanding channel and leave the microfluidic device.

The numerical simulations were carried out in a two–dimensional (2D) domain. The commercial simulation software Comsol Multiphysics 4.2 was adopted to solve the governing equations shown in Section 2.1, 2.2 and 2.3. For the fluid domain, all the inlets were specified with the average velocities which were calculated from Q_c and Q_d used by the experiments[13]. The outlet was specified as the pressure outlet without viscous stress. All the wall boundaries were imposed with the wetted wall conditions, for which a contact angle of 145° was assigned. When the fluid interface contacts the channel wall, such implementation enforces the slip condition to the wall boundaries that the interface can move along the wall. According to the previous studies, the effect of changing the contact angle has negligible effect on the droplet breakup process[6, 37]. For the electrostatic domain, the left side inlet was specified with electric potential as V_0. The right side inlet was specified with electric potential as 0. The other boundaries were specified with zero free charge condition which is expressed as

$$\hat{\boldsymbol{n}} \cdot (\varepsilon^* \boldsymbol{E}^*) = 0 \tag{18}$$

in which $\hat{\boldsymbol{n}}$ is the normal of the boundary; ε^* is the electric permittivity of the fluid close to the boundary.

After a mesh dependence study was performed with respect to several computational meshes of various resolutions, a computational mesh consisting of 16 nodes across the orifice and 13,160 elements totally in the entire domain was selected for the following numerical

investigations. In the first part of this study, no electric field was applied to the microfluidic system. The inlet of the dispersed phase maintained the averaged velocity as 6.460×10^{-4} m/s, corresponding to Q_d = 0.04 mL/h in the experiments; meanwhile, the inlet velocity of the continuous phase was varied to investigate the effect of fluid hydrodynamics on droplet breakup processes. In the second part, the inlet velocities of the dispersed and continuous phases maintained constant values as 6.460×10^{-4} m/s and 1.293×10^{-2} m/s, respectively, for all the cases, which corresponds to Q_d = 0.04 mL/h and Q_c = 50 Q_d in the experiments. External electric fields with various strengths were applied to the microfluidic system by varying the applied voltages from 10 V to 660 V.

The properties of the two phases used in the simulations are listed in Table 1. Two types of silicone oil with μ_d = 50 cp and 100 cp were used by the dispersed phase. The interfacial tension coefficient between the two phases was assumed to maintain a constant value as σ = 4.8 mN/m for all the investigated cases. The small variations of the density and interfacial tension between the two types of silicone oil were neglected.
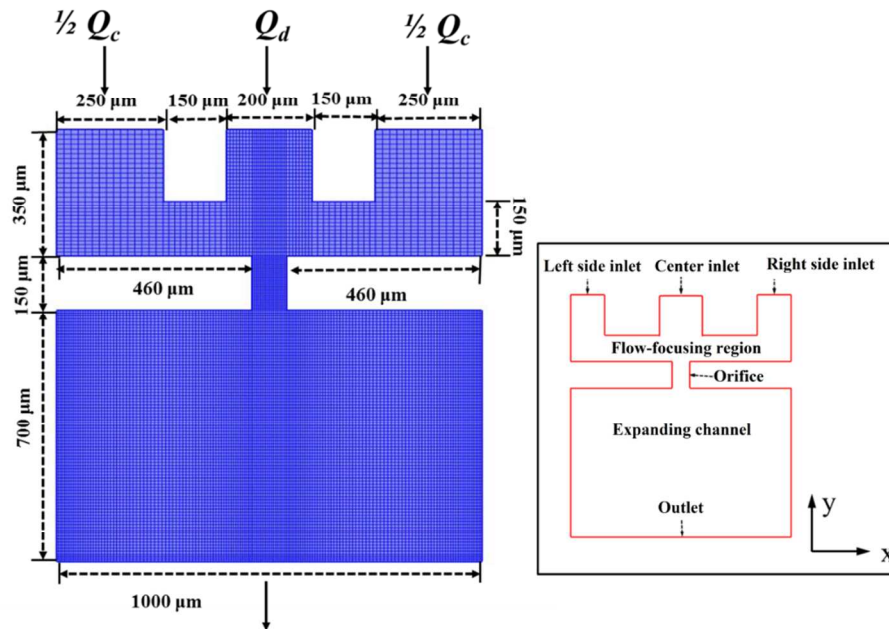

Figure 1 The geometry and dimensions of the microfluidic hydrodynamic flow–focusing device (HFFD) used in this study. The channels have uniform depths as 86 μm. The width and length of

the orifice are 80 μm and 150 μm, respectively. The blue lines indicate the computational mesh
used in the simulations.

Table 1 Properties of the two phases

Liquids	Continuous phase	Dispersed phase
Density (kg/m^3)	1000	960
Viscosity (mPa*s)	1	50/100
Permittivity (C/(V*m))	78.5×8.854×10^{-12}	2.8×8.854×10^{-12}
Interfacial tension (N/m)	0.0048	

3. Results and Discussion

3.1 Droplet formation process without electric field

3.1.1 Validation of the numerical model

In order to validate the accuracy of the conservative level–set model, numerical
simulations were carried out to study the droplet breakup process solely governed by the fluid
flow. The experimental work has been performed by Nie *et al.* in 2008[13]. In their work, they
maintained a constant flow rate of the dispersed phase (Q_d = 0.04 mL/h) while varying the flow
ratios of the continuous phase to the dispersed phase (Q_c/Q_d) in a wide range. For a particular
operating flow ratio, Q_c/Q_d = 20, the corresponding capillary number of the continuous phase Ca_c
is 0.0067 ($Ca_c = We_c/Re_c = u_c\mu_c/\sigma$). As Ca_c represents the ratio of the viscous shear forces to
the interfacial tension force, the small value of Ca_c indicates that the breaking mechanism is
primarily governed by the "squeezing" mechanism[38] or referred as "dripping regime–model 1" by
Nie[13].

Based on the flow rates and the cross sectional areas of the inlets, the average inlet
velocities were estimated and supplied to the simulations. As evident in Figure 2, the snapshots of
the droplet breakup processes predicted by the simulations agree qualitatively with the
observations from the experiments. The two cases shown in Figure 2 have same operating
conditions (Ca_c and Q_c/Q_d) but different ratios (μ_d/μ_c). Nie *et al.* have pointed out that the
viscosity ratio of the two phases plays a significant role in determining the droplet breakup modes.
They observed the mono–dispersed breakup mode when silicone oil with 20 cp was used as the

13

dispersed phase. As seen in Figure 2(A), the pendant blocks the entire exit of the orifice while it is growing on the front tip of the dispersed phase. While the continuous phase squeezes the dispersed phase, a visible "neck" shape is formed inside the orifice. For this case, only one droplet is pinched off from the dispersed phase. In contrast, the dispersed phase with $\mu_d = 100$ cp results in poly–dispersed breakup mode. As shown in Figure 2(B), the dispersed phase does not block the orifice exit completely in this case; besides, it forms a thin filament inside the orifice. After the primary droplet is pinched off, several secondary droplets with much smaller sizes are generated from the filament. The numerical simulations have predicted these two breakup modes successfully.

The numerical simulations have also achieved quantitative agreements with the experimental observations in terms of primary droplet sizes. We have studied the droplet breakup process with two types of viscosity ratios: $\mu_d/\mu_c = 50$ and 100, respectively. The predicted droplet diameters in the dimensionless form ($D^* = D_p/w_o$, of which D_p is the actual droplet sizes) as a function of Q_c/Q_d are plotted in Figure 3. The circular symbols represent numerical results predicted by numerical simulations while the square symbols stand for experiment data reported by Nie et al[13]. As seen in Figure 3, the primary droplet sizes predicted by the simulations are close to the experimental results. One may notice that the primary droplet sizes do not decrease noticeably by increasing flow ratios, which suggests that the conventional approach to manipulate droplet sizes by tuning the flow ratio is not effective in these circumstances. Other approaches are necessary in order to control the droplet sizes in such cases.

The conventional HFFDs have been observed to be ineffective to control the droplet sizes when μ_d is much larger than μ_c. And the physical explanations have not been provided by the experimental study. In order to understand the root causes, we have investigated them with the aid of simulations in Section 3.1.2 and 3.1.3.
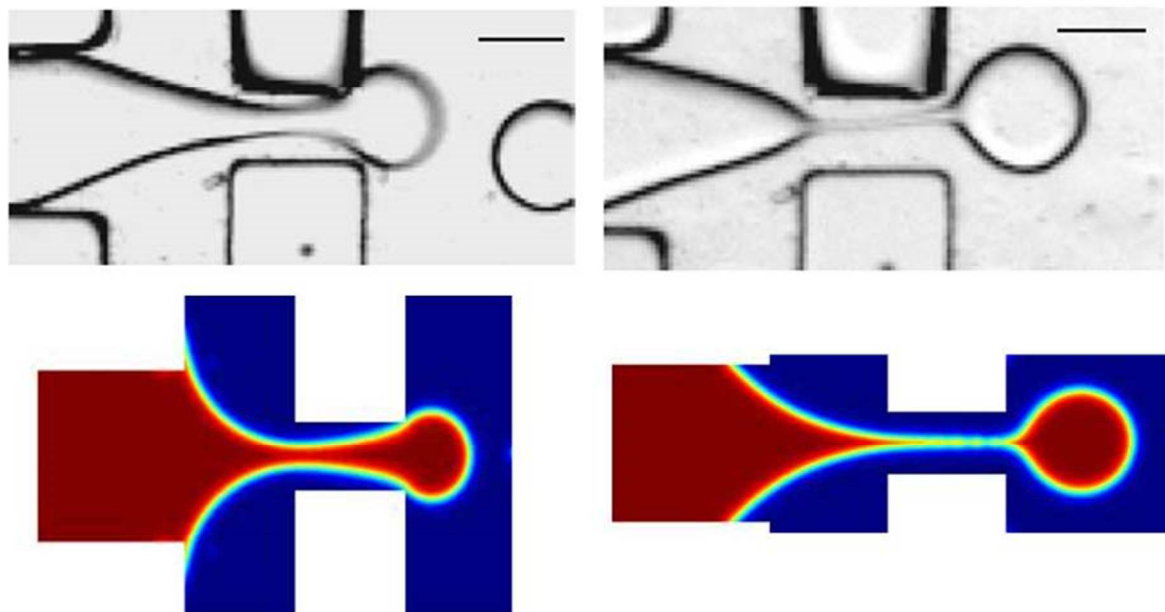
Figure 2 Snapshots of the droplet breakup process with different viscosity values of the dispersed phase: (a) $\mu_d/\mu_c = 20$ (b) $\mu_d/\mu_c = 100$. The flow ratios Q_c/Q_d in these two cases are 20, and the corresponding Ca_c are 0.0067. The upper pictures are the snapshots cited from the experiments performed by Nie *et al.*[13]. The scale bars indicated as the black lines are 100 μm. The lower pictures are provided by the numerical simulations.
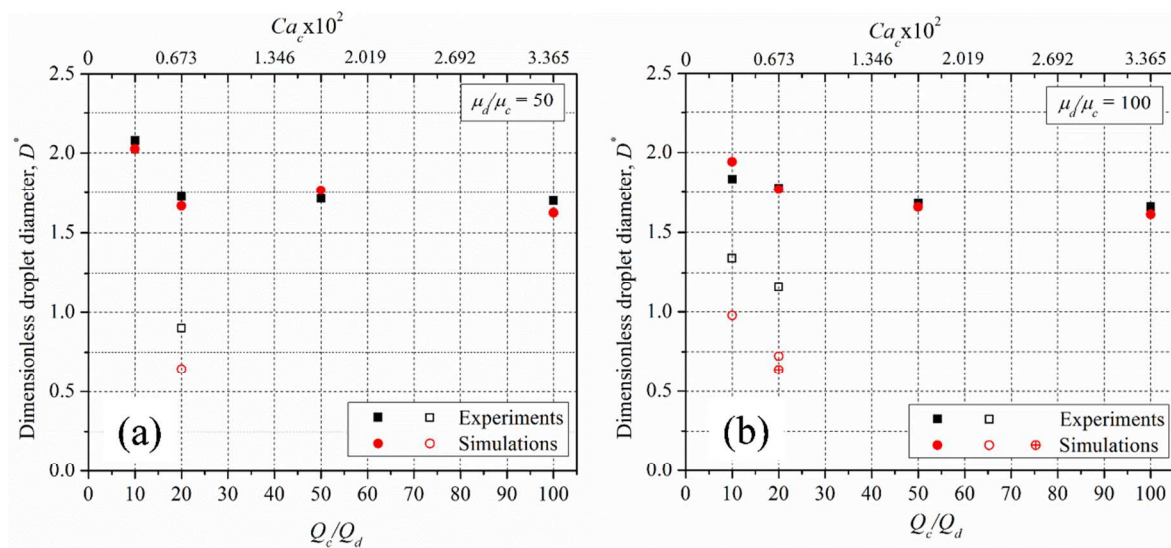

Figure 3 The dimensionless droplet sizes D^* as a function of flow ratios Q_c/Q_d at viscosity ratio: (a) $\mu_d/\mu_c = 50$; (b) $\mu_d/\mu_c = 100$. The filled symbols represent the primary droplets while the open symbols stand for the secondary droplets produced by the poly–dispersed breakup mode. If multiple secondary droplets are produced, only two of them are plotted for the purpose of showing the general size range. The experimental results are cited from Nie's work[13].

3.1.2 Droplet breakup process in the dripping regime

The numerical investigations in this study focus on the dripping regime where the droplets were generated by the mono–dispersed breakup mode. In this section, we demonstrate a typical droplet formation process that is solely governed by the hydrodynamics of fluid flow. The corresponding operating conditions are: $\mu_d/\mu_c = 50$, $Q_c/Q_d = 50$ and $Ca_c = 0.017$. The relatively large Ca_c indicates that the breakup process is governed by the "dripping" mechanism[38]. The corresponding Reynolds number of dispersed phase is 0.0025 ($Re_d = \rho_d u_d w_o/\mu_d$, u_d is the mean velocity of the dispersed phase in the orifice region, which is estimated by dividing the flow rate of the dispersed phase with the cross–sectional area of the orifice).

The predicted droplet breakup process from the numerical simulation is plotted in Figure 4. When external forces are absent, three forces play primary roles in the breakup process. Namely, they are the surface tension force, the viscous shear force and the upstream pressure force across the fluid interface[11]. Due to the complexity of the dynamic breakup process, the magnitudes of surface tension force and viscous shear force vary with respect to time and locations. In order to understand the upstream pressure force qualitatively, the evolutions of the pressure values in the upstream of the orifice, which are abbreviated as *upstream pressure evolutions* in the following text, were measured from two phase during the breakup process. The dimensionless pressure p^* is plotted as a function of dimensionless time t^* in Figure 5. The sampling locations in the continuous phase and the dispersed phase are indicated by the circle and diamond symbols as seen in Figure 4(a).
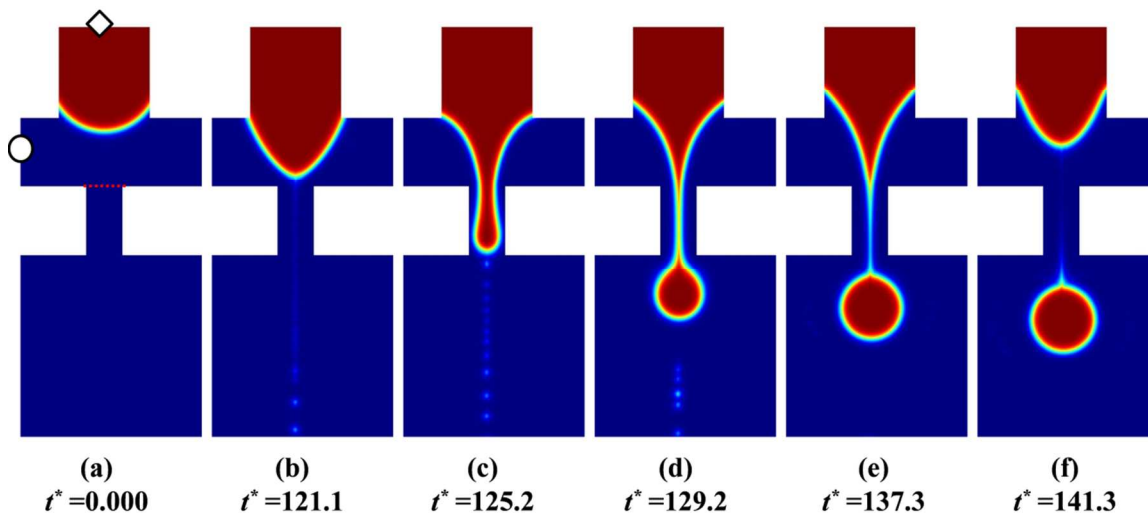
(a)   (b)   (c)   (d)   (e)   (f)
t^* =0.000 t^* =121.1 t^* =125.2 t^* =129.2 t^* =137.3 t^* =141.3

Figure 4 Droplet formation process in the dripping regime with the operating condition: $\mu_d/\mu_c =$ 50, Q_c/Q_d= 50, Ca_c =0.017 and Re_d = 0.0025. The dimensionless time t^* is normalized by the time scale w_o/u_c. The diamond and circle symbols indicate the sampling locations where the upstream pressure values were measured.
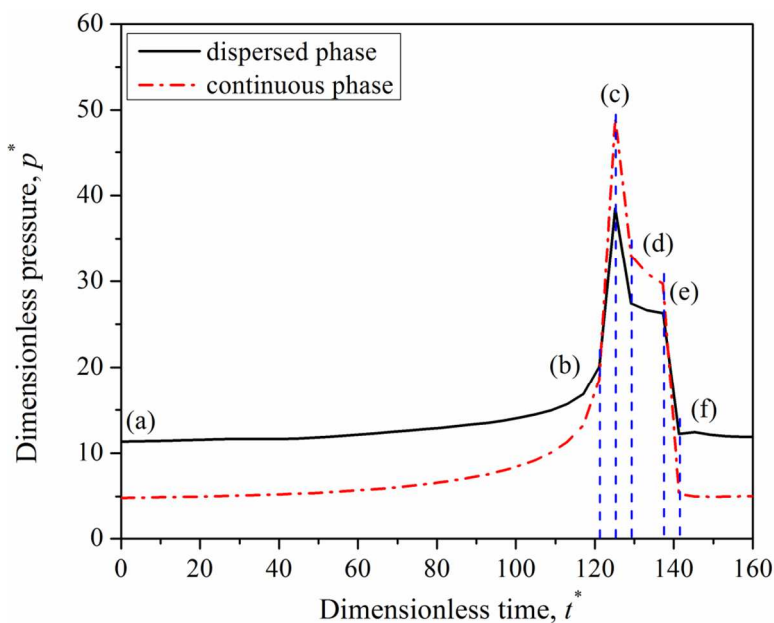

Figure 5 Evolution of the upstream pressure in the continuous phase and dispersed phase during the droplet breakup process with the operating conditions as μ_d/μ_c = 50, Q_c/Q_d= 50, Ca_c =0.017 and Re_d = 0.0025. The dimensionless time t^* is normalized by the time scale w_o/u_c. The dimensionless pressure p^* is normalized by the pressure scale $\rho_c u_c^2$. The (a) ~ (f) correspond to six steps shown in Figure 4. The solid line represents the pressure in the dispersed phase while the dash dot line stands for that in the continuous phase. The dash lines indicate the locations of the corresponding steps on the curves for the visualization purpose.

17

Generally, the droplet breakup process consists of two stages: the blocking stage and the squeezing stage. The detailed procedures of the droplet breakup process can be summarized as six steps. (a) The dispersed phase penetrates the continuous phase and travels towards the orifice from the center inlet. Because the viscosity of the dispersed phase is larger than that of the continuous phase, the dispersed phase maintains a higher pressure in its upstream than that of the continuous phase, which is evident between $t^* = 0$ and $t^* = 120$ in Figure 5. (b) As the dispersed phase enters the flow–focusing region, it gradually blocks the flowing channel of the continuous phase. In order to maintain its constant flow rate, the continuous phase has to increase its velocity, which consequently elevates its upstream pressure. The upstream pressure in the dispersed phase increases accordingly as well so as to penetrate the continuous phase. Thus the upstream pressure values in both phases increase gradually from step (a) to (b) with higher pressure values in the dispersed phase. When the tip of the dispersed phase reaches the orifice entrance, the fluid interface maintains a conical shape as seen in Figure 4(b), which is usually referred as the "Taylor cone". (c) As soon as the dispersed phase enters the orifice, the squeezing stage starts. The pressure values of both phases shoot up rapidly as a result of the confined flowing area inside the orifice. In this step the pressure value of the continuous phase exceeds that of the dispersed phase. When the tip of the dispersed phase reaches the orifice exit, the pressure curves of both phases reach their peaks. Because of the pressure difference between two phases, the continuous phase squeezes the fluid interface, which consequently forms a visible neck inside the orifice as shown in Figure 4(c). (d) When the tip of the dispersed phase leaves the orifice exit and enters the expanding channel, the pressure values in both phases decline suddenly because of the expanded flowing area. While the continuous phase keeps squeezing the interface, the neck in the orifice is compressed into a thin filament as seen in Figure 4(d). A pendant is growing in the expanding channel close to the orifice exit, with its tail attached to the dispersed phase by the filament. (e) As the continuous phase keeps exerting the compression effect, the width of the filament is reduced slowly. Because of the gradually increased flowing area inside the orifice, the upstream

18

pressure values in both phases decrease accordingly as well. (f) When the width of the filament is squeezed to a critical value, the surface tension force snaps off the pendant from the dispersed phase and brings the interface out of the flow–focusing region as seen in Figure 4(f). Consequently, a droplet of well–defined spherical shape is generated inside the expanding channel. The pressure values in both phases rapidly drop to those required by the initial step (a), with larger pressure in the dispersed phase than that in the continuous phase. A new cycle starts to repeat.

3.1.3 The effect of operating flow ratios on droplet sizes

For most of the applications using passive droplet–based microfluidics, manipulating the operating flow ratio is the primary approach to control droplet sizes. However, Figure 3 has suggested that increasing the flow ratio cannot lead to a noticeable reduction in droplet sizes. In order to understand the effect of operating flow ratios on the breakup process, we have analyzed the evolutions of the neck width (W_n^*) for two cases having different flow ratios (Q_c/Q_d =50 and 100, respectively). The other operating conditions are identical: Re_d = 0.0025 and μ_d/μ_c = 50. The neck width W_n^* was measured at the orifice entrance with respect to the dimensionless time t^* during the simulations, for which the sampling location is indicated as the dot line shown in Figure 4(a). The obtained evolution curves of W_n^* are shown in Figure 6.

Taking the case with Q_c/Q_d =50 as an example, the neck width W_n^* is zero initially during one cycle of the droplet breakup process. Then it reaches its maximum value at the end of the blocking stage when the dispersed phase enters the orifice (as shown in Figure 4(b)). Because of the strong squeezing effect resulting from the significant pressure difference between the two phases, W_n^* drops rapidly from step (b) to (d). After the tip of the dispersed phase enters the expanding channel, the squeezing effect is weakened from step (d) to (e) for two reasons. On one hand, the pressure difference between two phases is reduced, which is evident in Figure 5. On the other hand, the viscous lubrication effect stabilizes the neck. The squeezing process in the
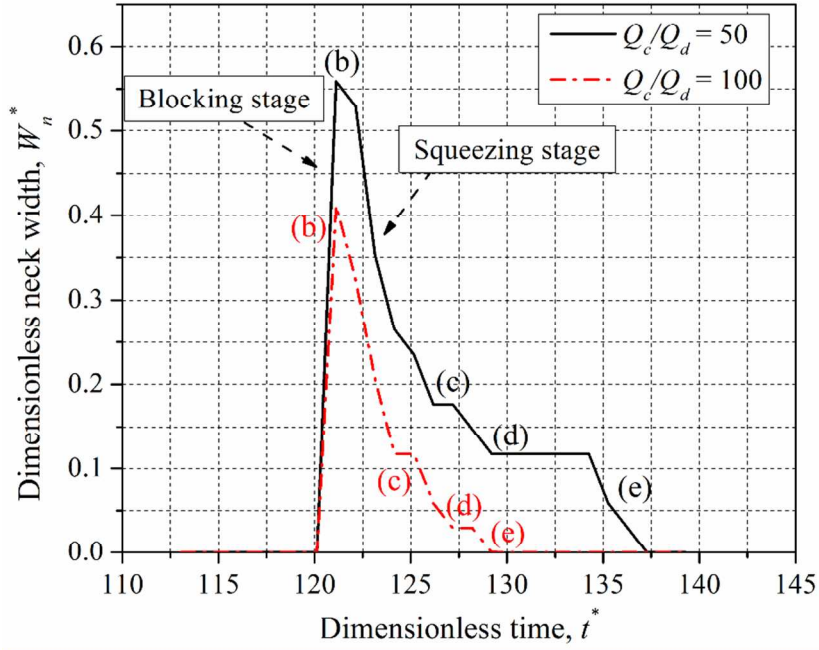
Figure 6 The evolution of neck width W_n^* measured from two cases with Q_c/Q_d= 50 and 100. The corresponding Ca_c are 0.017 and 0.034, respectively. The other operating conditions of these two cases are identical: Re_d = 0.0025 and μ_d/μ_c = 50. W_n^* is normalized by the orifice width w_o. The symbols (b) ~ (e) indicate the corresponding steps of the droplet breakup process shown in Figure 4.

squeezing stage is analogues to the classic "thinning of the fluid film pushed by two parallel discs". Following the classic Stefan-Reynolds relation[39], the magnitude of viscous resistance force in the orifice regime can be expressed as:

$$F_{resis} = \frac{3\pi\mu_d u_c L_o^4}{32 w_o^3} \left[\left(\frac{1}{W_n^*}\right)^3 \left(\frac{dW_n^*}{dt^*}\right) \right] \tag{19}$$

where L_o is the length of the orifice; dW_n^*/dt^* is the thinning rate of the neck with respect to time. This relation indicates that the viscous resistance force is proportional to $\left(\frac{1}{W_n^*}\right)^3$, thus the resistance force acting on the thin filament during step (d) to (e) is much stronger than that in previous steps. The weakened squeezing effect as well as the strengthened viscous lubrication effect maintained the thin fluid neck for a fairly long time, resulting in a tail shape of the

20

evolution curve. Finally, W_n^* returns to 0 when the droplet is pinched off (as shown in Figure 4(e)).

Increasing the flow ratio primarily provides two effects to the droplet breakup process. On one hand, the viscous shear force is strengthened according to the expression of Ca_c. On the other hand, the maximum neck width W_n^* is reduced during the blocking stage as the flow ratio increases, which is evident from Figure 6. However, even if the operating flow ratio is doubled, the resultant droplet sizes from these two cases are still close to each other. By comparing the corresponding evolution curves shown in Figure 6, one may notice that the slopes of the curves from step (b) to (d) are almost same. As these slopes can be regarded as the squeezing rate, such results reveal that the squeezing rate cannot be accelerated by increasing the flow ratio due to the viscous lubrication effect. An effective way to reduce the droplet sizes is to employ external forces such as the electric force to accelerate the squeezing process.

3.2 Droplet breakup process controlled by the electric field

3.2.1 Validation of the perfect dielectric model by the classic drop deformation

Before utilizing the electric field to control the droplet breakup process, we simulated one case of the classic droplet deformation problem for the purpose of validating the LSM coupled with the electrostatic model. It is well known that a fluid droplet suspended inside another immiscible fluid deforms with the presence of external electric field[31]. The deformation parameter, d, is generally defined as:

$$d = \frac{b-a}{b+a} \tag{20}$$

in which a is the equatorial radius of the spheroid and b is the polar half–axis. The resultant deformation is a function of interfacial tension, fluid properties of the both phases (such as viscosity, permittivity and conductivity), and the magnitude of the applied electric field. O'Konski and Thacher have derived the analytical expression that can predict the steady–state deformation of a dielectric droplet, d_∞, in another dielectric media[40]:

$$d_\infty = \frac{R_0 \varepsilon_c}{\sigma} |E_0|^2 \frac{9(S-1)^2}{16(S+2)^2} \tag{21}$$

in the tested case, R_0=1 mm is the non–deformed droplet diameter; ε_c= ε_0 is the dielectric permittivity of the suspending medium; $\sigma = 0.0032$ N/m is the interfacial tension coefficient; $E_0 =$ 1.5×10^5 V/m is the magnitude of the electric field far from the droplet; the parameter S represents the ratio of the dielectric permittivity of the droplet (ε_d =10 ε_0) to that of the suspending medium.

If these parameters are provided to the analytical expression, the deformation of the droplet in steady state is $d_\infty = 0.0197$. The same parameters were also adopted by the numerical simulations carried out in a 2D-axisymmetric domain. The details about the simulation setup are provided in Appendix B. When the electric field is absent, the droplet preserves its spherical shape. After the deformation of the droplet reaches the steady state inside the electric field, the deformed shape of the droplet is shown in Figure 7(b). Estimated by Eq. (20), the corresponding deformation value in steady state predicted by the numerical simulation is 0.0214, which agrees well with the analytical solution.

In addition, the dynamic response curve of the deformation process shown in Figure 7(a) has a similar shape as that reported by Supeene et al[31]. Therefore, the numerical model using LSM coupled with the perfect dielectric model is regarded as sufficiently reliable to study the droplet breakup process in the following sections.
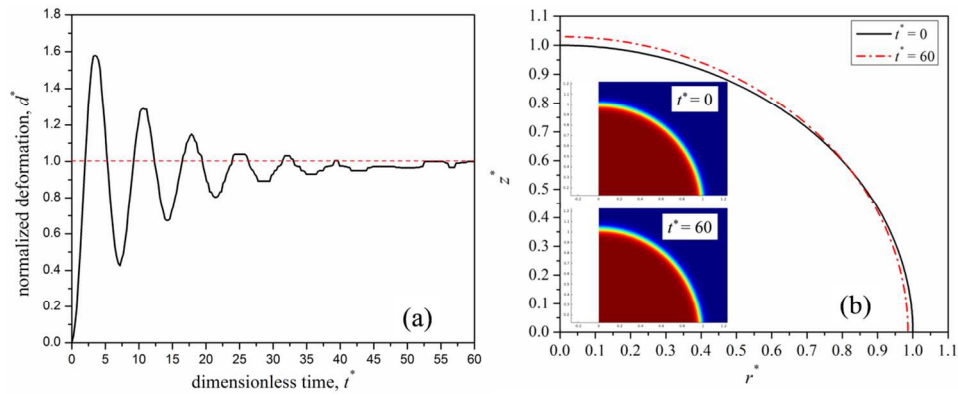

Figure 7 (a) The dynamic response curve of the droplet deformation caused by the external electric field. The dimensionless time t^* is scaled with respect to the characteristic time scale for oscillation of an inviscid droplet[31, 41]. The deformation is normalized as: $d^* = d/0.0214$ (b) The

shape of the droplet before deformation $t^* = 0$ and in the steady state $t^* = 60$. The line plots sketch the shape of the droplet by plotting the contour line with $\phi = 0.5$.

3.2.2 Overview of the electric field strength on droplet breakup process

As seen in Figure 8(a), the external electric field is applied to the microfluidic system in such a way that the left side inlet is attached to a DC power supply while the right side inlet is connected to the ground. Such configuration induces polarization charges on the fluid interface thus generates electric field inside both phases. As suggested by the continuity of the electric displacement shown in Eq. (17), the magnitude of the electric field strength in the dispersed phase is larger than that in the continuous phase since ε_d is less than ε_c. The numerical simulations have captured such phenomenon. The contour plot of the electric field strength shown in Figure 8(a) reveals that the electric field with large strength exists in the front tip of the dispersed phase. The thinner width of the fluid neck, the stronger electric field is generated inside the dispersed phase. Because of the interactions between the electric field and the polarization charges, the electric force is induced on the fluid interface, of which the distributions are plotted as the white arrows shown in Figure 8(b). As the direction of the electric force is determined by the gradient of the permittivity values ($\nabla \varepsilon^*$) as seen in Eq. (15), the flow configuration such that ε_d is less than ε_c results in the electric force always pointing from the continuous phase towards the dispersed phase. If the force vectors are decomposed along x and y directions, one may notice that the force component on x direction exerts a compression effect to the dispersed phase; consequently, it overcomes the viscous lubrication effect and helps to squeeze the neck of the dispersed phase during the drop breakup process. On the other hand, the force component along the y direction is pointing opposite to the moving direction of the dispersed phase, thus it retards the movement of the interface to the orifice.

In order to understand the effect of electric field strength on the resultant droplets sizes, the droplet breakup processes with two types of viscosity ratios ($\mu_d/\mu_c = 50$ and 100) were studied with constant flow rates of the two phases ($Q_c/Q_d = 50$ and $Ca_c = 0.017$) but varying values of the

applied voltages V_0 on the left side inlet. V_0 was varied from 10 to 660 V, corresponding to $Eu^{-1/2}$

in the range between 0.095 and 5.24. The normalized droplet sizes and droplet periods predicted

from the numerical simulations are plotted as functions of $Eu^{-1/2}$ in Figure 9(a) and (b).

Interestingly, the curves of droplet sizes versus $Eu^{-1/2}$ exhibit the descending–ascending–

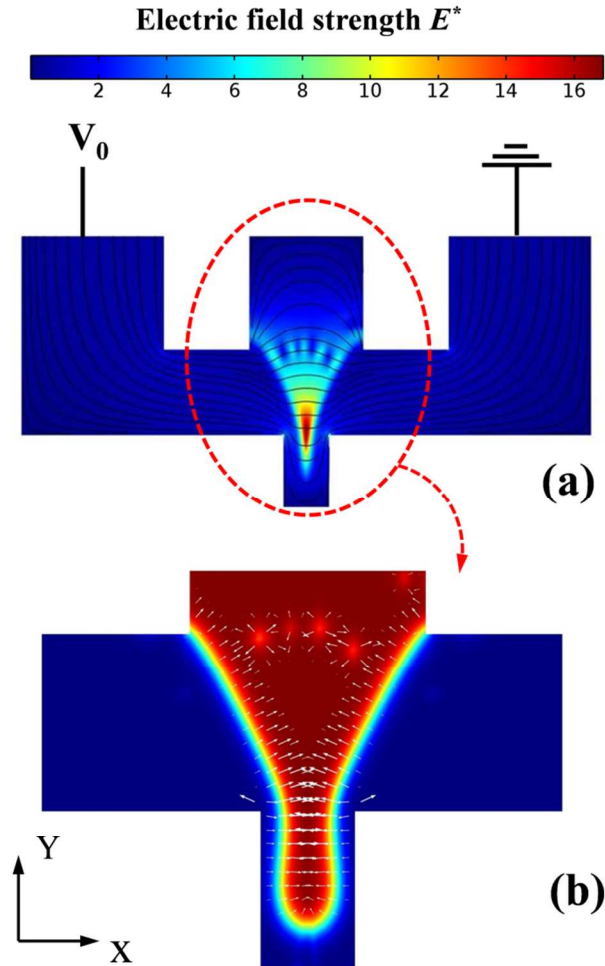descending shapes instead of the monotonously descending shape.

Figure 8 (a) Contour plot of the electric field strength at one time step during the droplet formation with $\mu_d/\mu_c = 50$, $Q_c/Q_d = 50$ and $Ca_c = 0.017$. The black lines indicate the electric field lines. In this case, $V_0 = 240$ V is applied to the left side inlet, corresponding to $Eu^{-1/2} = 1.906$. The color map indicates the magnitude of the scaled electric field strength $E^* = E/E_0$. (b) Contour plot of the volume fraction of the dispersed phase in the regions enclosed by the red dash curves shown in (a). The white arrows indicate the vectors of the electric body force induced on the fluid interface.

The droplet period, which is defined as the time interval between the formations of two adjacent

droplets, follows the similar trend as that of the droplet size. According to the shape of the curves

shown in Figure 9, the droplet breakup process, controlled by the electric field of various

strengths, can be divided into three distinct regimes. In Regime 1 where $Eu^{-1/2}$ ranges between 0

and 2.38, the droplet sizes and periods decrease almost linearly with increasing values of $Eu^{-1/2}$.

Similar relationships of the droplet sizes and applied voltages have also been reported by Link[19]

Kim[24], and Yeh[42] individually based on their experiments on aqueous droplet–in–oil systems. If

$Eu^{-1/2}$ is between 2.38 and 3.81, the droplet breakup process is governed by Regime 2 where the

droplet sizes and periods increase with $Eu^{-1/2}$. In Regime 3 where $Eu^{-1/2}$ exceeds 3.81, the droplet

sizes and periods decrease almost linearly with V_0 again. Such breakup patterns are resulted from

the interactions of the electric force and the fluid flow in the microfluidic system. In the following

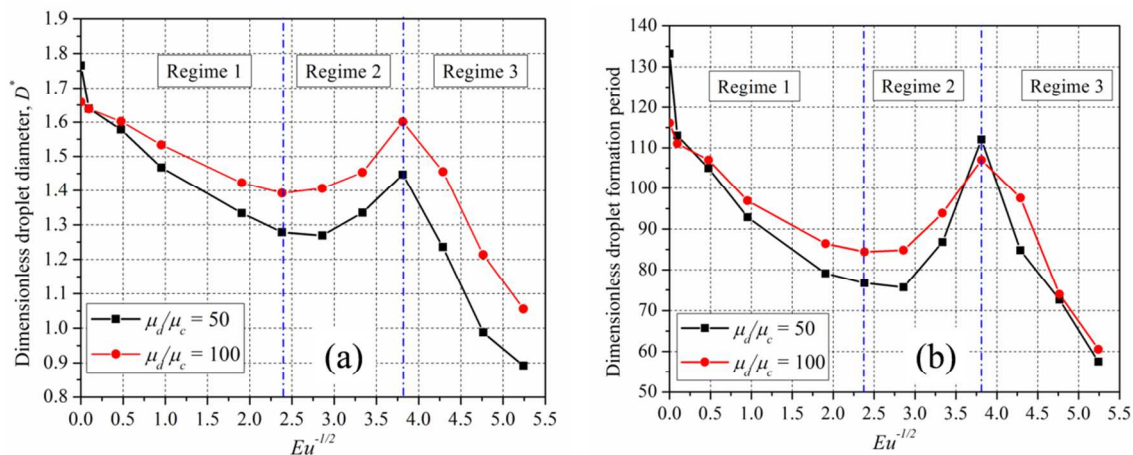sections, the droplet breakup processes in these individual regimes are discussed one by one.

Figure 9 (a) Normalized droplet diameters D^* as a function of $Eu^{-1/2}$. (b) Normalized droplet period as a function of $Eu^{-1/2}$. The time scale with respect to the droplet period is w_o/u_c. The other operating conditions used in the simulations are: $Q_c/Q_d = 50$ and $Ca_c = 0.017$.

3.2.3 Droplet breakup process in Regime 1

In Regime 1, the droplet sizes and periods decrease almost linearly with the increase of

the applied voltage $Eu^{-1/2}$. The contour plots of the droplet breakup process for two cases in this

regime are shown in Figure 10. These two cases have identical operating conditions but different

applied voltages, the corresponding values of $Eu^{-1/2}$ are 0.477 and 1.906, respectively. By

comparing (b1) and (b2) in Figure 10, one may notice that the dispersed phase deforms inside the flow–focusing region noticeably if $Eu^{-1/2}$ increases to 1.906. Such deformation is resulted from the y component of the electric force, which retards the movement of the dispersed phase by exerting the force opposite to the flow direction. In addition to the deformation, the dispersed phase has to spend more time during the blocking stage as $Eu^{-1/2}$ increases, which is evident by comparing the time interval between (a1), (b1) and (a2), (b2).
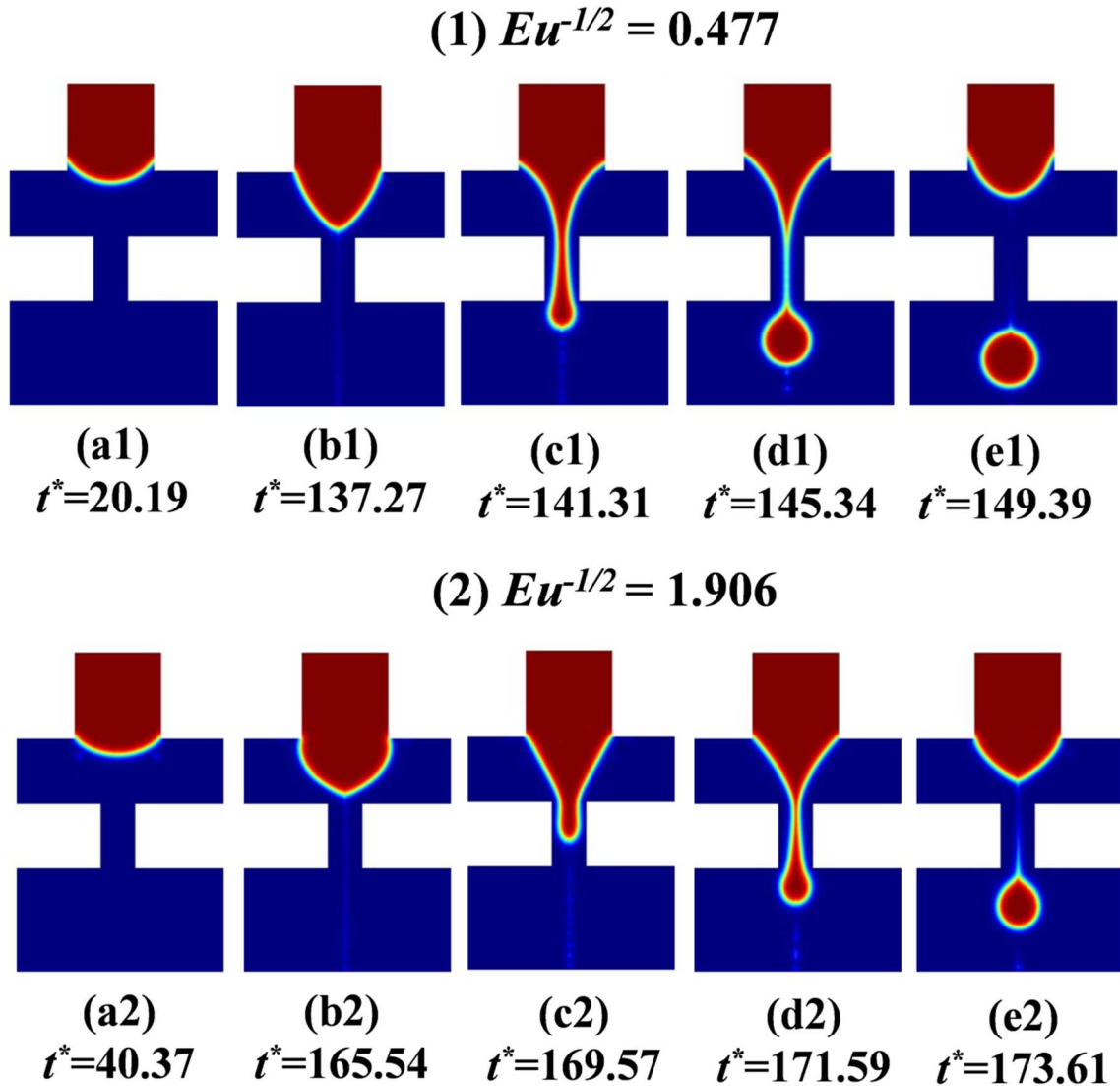
(1) $Eu^{-1/2} = 0.477$

(a1)	(b1)	(c1)	(d1)	(e1)
t^*=20.19	t^*=137.27	t^*=141.31	t^*=145.34	t^*=149.39

(2) $Eu^{-1/2} = 1.906$

(a2)	(b2)	(c2)	(d2)	(e2)
t^*=40.37	t^*=165.54	t^*=169.57	t^*=171.59	t^*=173.61

Figure 10 Two examples of the droplet breakup process in Regime 1 with identical operating conditions as μ_d/μ_c =50, Q_c/Q_d = 50 and Ca_c = 0.017. The applied voltages V_0 are 60 V and 240 V, respectively, corresponding to $Eu^{-1/2}$ values as 0.477 and 1.906. (a1) ~ (e1): droplet breakup

process with respect to $Eu^{-1/2} = 0.477$; (a2) ~ (e2): droplet breakup process with respect to $Eu^{-1/2} =$ 1.906.

On the other hand, the component of the electric force along the x direction overcomes the viscous lubrication effect and helps to squeeze the dispersed phase, resulting in the enhanced squeezing rate during the squeezing stage. Compared to the breakup process without electric field shown in Figure 4, the dimensionless squeezing time from step (b) to (e) is reduced from 20.2 to 12.1 if $Eu^{-1/2} = 0.477$ is applied to the system. As the droplet growing time is shortened by applying the external squeezing force, the dimensionless droplet size is consequently reduced from 1.77 to 1.58. If $Eu^{-1/2}$ is further increased to 1.906, the time interval required by the squeezing stage is shortened to 8, which eventually reduces the averaged droplet sizes to 1.33.
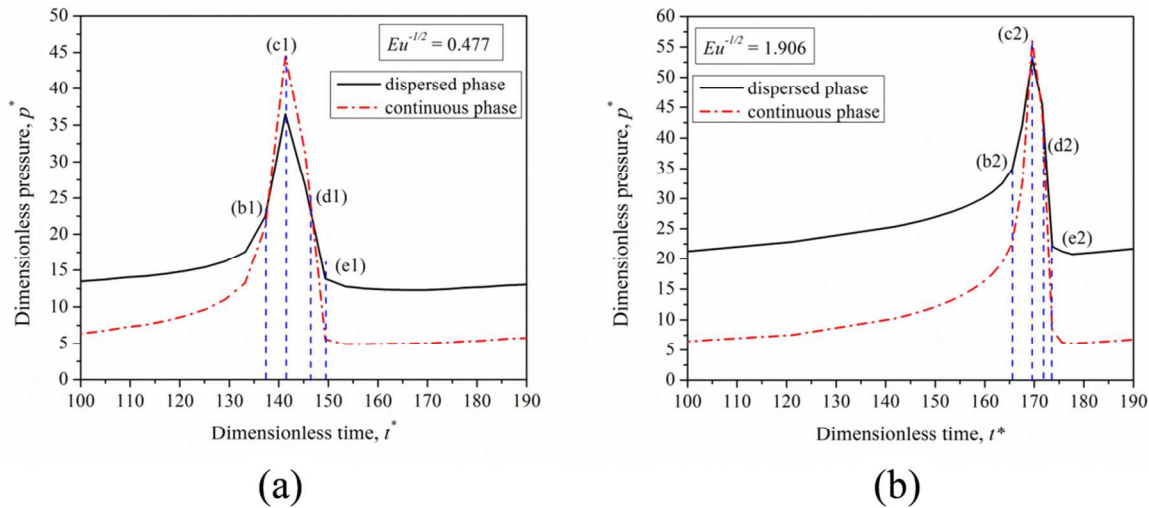

Figure 11 Evolution of dimensionless upstream pressure, p^*, in the continuous and dispersed phases during the droplet breakup process with the operating conditions: $\mu_d/\mu_c = 50$, $Q_c/Q_d = 50$ and $Ca_c = 0.017$. (a) $Eu^{-1/2} = 0.477$; (b) $Eu^{-1/2} = 1.906$. (b1) ~ (e1) and (b2) ~ (e2) correspond to the droplet breakup steps shown in Figure 10. The blue dot lines indicate the location of corresponding steps shown on the curves.

Since the dispersed phase has to overcome the retardation effect exerted by the y component of the electric force, a high pressure value has to be built up in its upstream so as to maintain the constant flow rate. By comparing the upstream pressure evolutions of the two phases shown in Figure 11(a) with those in Figure 5, one may notice that the pressure values in the dispersed phase have increased noticeably for the entire time range as $Eu^{-1/2} = 0.477$ is applied to

the system. Meanwhile, the pressure values in the continuous phase are marginally influenced by the electric field. As a result of the increased pressure in the dispersed phase, the squeezing effect contributed by the hydrodynamics of fluid flow is undermined; in other words, the squeezing effect that is contributed by the pressure difference between the two phases is weakened. If $Eu^{-1/2}$ is further increased to 1.906, the pressure values in the dispersed phase have increased significantly as seen in Figure 11(b). The pressure difference between the two phases from step (c) to (e) is so small that the squeezing effect contributed by the hydrodynamics of fluid flow is negligible compared to that contributed by the electric force. One may expect that the squeezing effect depends solely on the electric force if $Eu^{-1/2}$ exceeds 1.906.

3.2.4 Droplet breakup process in Regime 2

When $Eu^{-1/2}$ ranges between 2.38 and 3.81, the droplet breakup process is governed by Regime 2 where the resultant droplet sizes increase with $Eu^{-1/2}$. A typical droplet breakup process in this Regime is plotted in Figure 12 while the corresponding upstream pressure evolution curves of the two phases are plotted in Figure 13. Because of the excessive retardation effect exerted by the electric field, the dispersed phase deforms considerably in the flow–focusing region during the blocking stage which is clearly shown in Figure 11(b). Such deformations of the dielectric fluid resulting from external DC fields are coincident with the classic drop deformation theory; similar deformed shapes of silicone oil inside air have also been observed by Zhang *et al.* in their experiments[43]. In order to overcome this strong retardation effect, the upstream pressure in the dispersed phase elevates noticeably during the entire breakup process; in comparison, the pressure in the continuous phase only has a small increment. As a result, the pressure in the dispersed phase overwhelms that in the continuous phase for the entire droplet breakup process as evident in Figure 13.
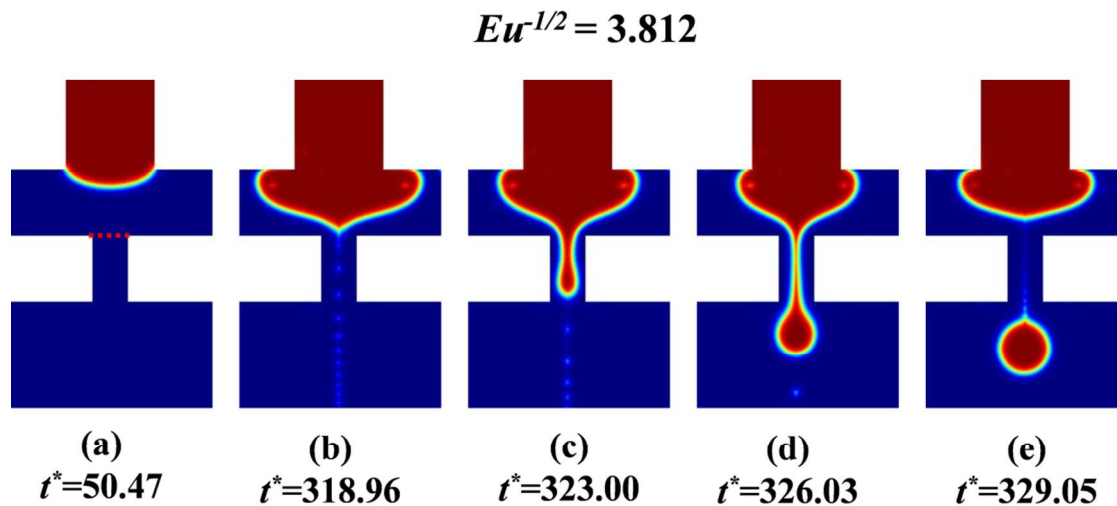
$Eu^{-1/2} = 3.812$

(a) $t^*=50.47$ (b) $t^*=318.96$ (c) $t^*=323.00$ (d) $t^*=326.03$ (e) $t^*=329.05$

Figure 12 A typical droplet breakup process in Regime 2 with $\mu_d/\mu_c = 50$, $Q_c/Q_d = 50$ and $Ca_c = 0.017$. The applied voltage V_0 is 480 V, corresponding to $Eu^{-1/2} = 3.812$.
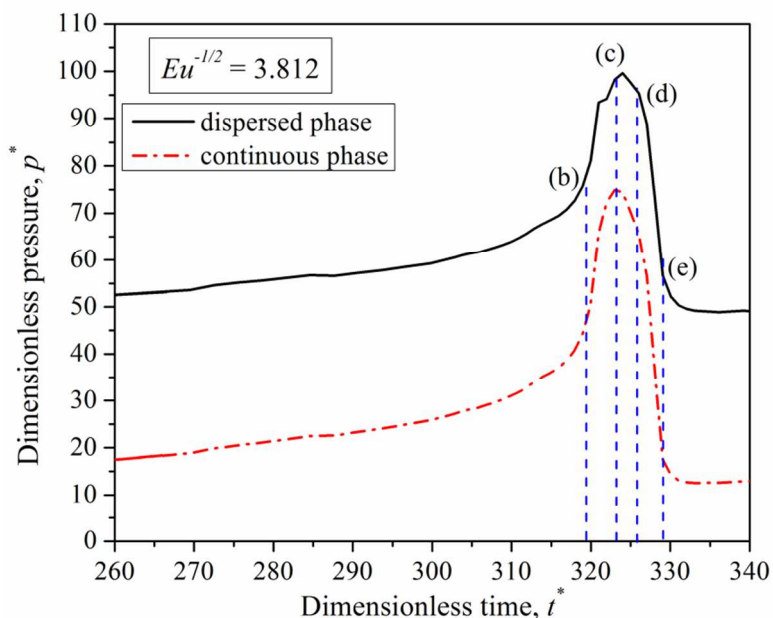

Figure 13 Evolution of dimensionless upstream pressure, p^*, in the continuous and dispersed phases during the droplet breakup process with the operating conditions: $\mu_d/\mu_c = 50$, $Q_c/Q_d = 50$ and $Ca_c = 0.017$. The applied voltage V_0 is 480 V, corresponding to $Eu^{-1/2} = 3.812$. (b) ~ (e) correspond to the droplet breakup steps shown in Figure 12. The blue dot lines indicate the location of corresponding steps shown on the curves.

During the squeezing stage (from step (c) to (e) shown in Fig. 12) of the breakup process,

two mechanisms are competing: one is the squeezing mechanism which is solely contributed by

the electric force; the other is the stabilization mechanism due to the retardation effect. In order to

overcome the retardation effect, the dispersed phase develops high pressure values in its upstream, which consequently expands the interface outwards thus stabilize the interface. Because of such stabilization effect, the squeezing time interval from stage (c) to (e) in the case with $Eu^{-1/2}$ = 3.812 is prolonged compared to that with $Eu^{-1/2}$ = 1.906, resulting in droplets with larger sizes as seen in Figure 10 and Figure 12. Similar evidence can be observed from the evolution curves of the dimensionless neck width, W_n^{*}, which were measured at the orifice entrance as well. As shown in Figure 14, the slope of the right half of the neck evolution curves, which is considered as the squeezing rate, is increased when $Eu^{-1/2}$ is raised from 0.095 to 2.859; as a result, the dimensionless squeezing time intervals of the corresponding cases are reduced from 10 to 4. However, if $Eu^{-1/2}$ is further increased to 3.812, the slope of the curve is decreased because of the stabilization effect, which substantially prolongs the squeezing time interval to 6. Similar stabilization effects have also been observed in other systems with the usages of strong DC fields. Kim *et al.* have applied a DC field to control the droplet breakup process of water (dispersed phase) in oil (continuous phase). They found that the electric field could reduce the droplet sizes if the applied voltages were less than certain critical values, *i.e.*, 1200 V in the case with Q_c/Q_d = 350/60. If the applied voltage increased to 1300 V, no droplets were pinched off from the dispersed phase; instead, the dispersed phase formed a stable jet, which propagated downstream without breaking into droplets in the orifice region[24].
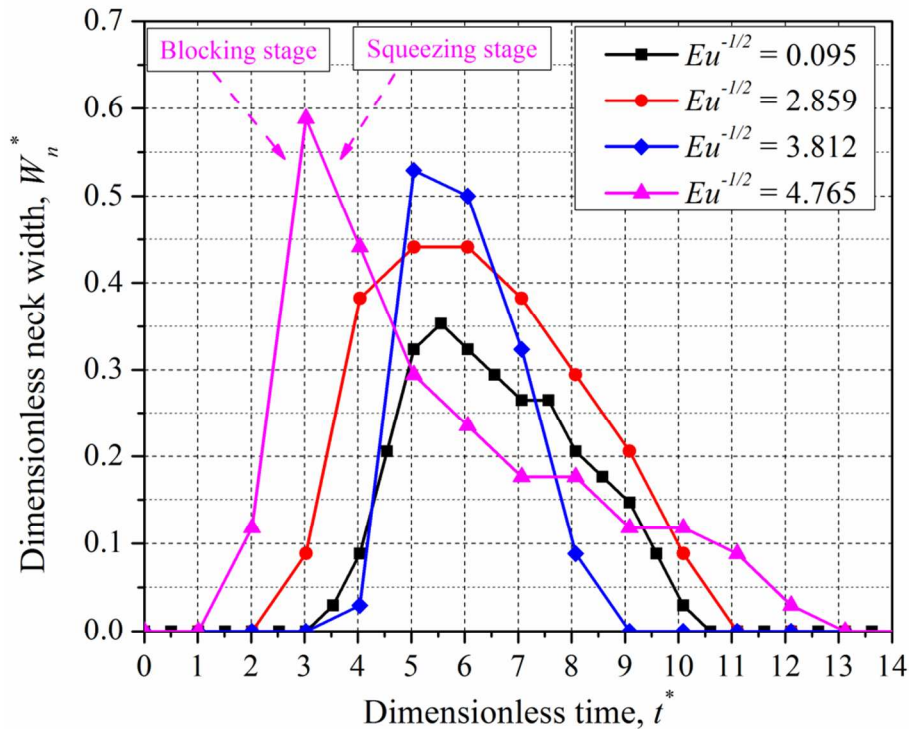
Figure 14 The evolution curves of the dimensionless neck width W_n^* measured from the orifice entrance from the cases with the operating conditions: $\mu_d/\mu_c = 50$, $Q_c/Q_d = 50$ and $Ca_c = 0.017$. Various applied voltages are applied to the system, corresponding to $Eu^{-1/2}$ between 0.095 and 4.765. The sampling location is marked by the red dash line shown in Figure 12(a).

3.2.5 Droplet breakup process in Regime 3

If very strong electric fields are applied to the microfluidic system, *i.e.*, $Eu^{-1/2} > 3.81$, the droplet breakup process is governed by Regime 3 where the resultant droplet sizes decrease with $Eu^{-1/2}$ again. A typical droplet breakup process with $Eu^{-1/2} = 4.765$ in this regime is shown in Figure 15, and the corresponding upstream pressure evolution curves are shown in Figure 16. Because of the significant retardation effect exerted by the strong electric force, the pressure in the dispersed phase overwhelms that in the continuous phase remarkably, which leads to a broad deformation of the dispersed phase in the flow–focusing region as seen in Figure 15(b). During the squeezing stage, a thin jet evolves from the apex of the dispersed phase and is elongated inside the orifice as seen in Figure 15(c) and (d). The formation and movement of the thin jet inside the microfluidic device is similar to that been observed by Zhang *et al.* in their experiments.

31

Zhang *et al.* have investigated the flow behavior of silicone oil in an external electric field, and they observed the formation of oil jets when the flow was governed by dripping regime and the applied electric voltage exceeded 9 kV. They pointed out these jets were unsteady and were initiated by the large electric field strength[43].

$$Eu^{-1/2} = 4.765$$

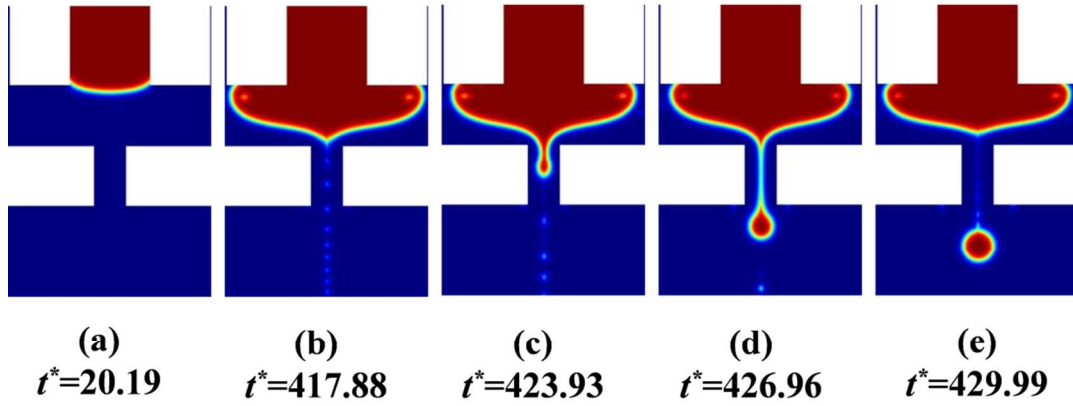| (a)	(b)	(c)	(d)	(e)
$t^*=20.19$	$t^*=417.88$	$t^*=423.93$	$t^*=426.96$	$t^*=429.99$

Figure 15 A typical droplet breakup process in Regime 3 with $\mu_d/\mu_c = 50$, $Q_c/Q_d = 50$ and $Ca_c = 0.017$. The applied voltage V_0 is 600 V, corresponding to $Eu^{-1/2} = 4.765$.

As seen in Figure 15(b), the significant deformation of the dispersed phase blocks most of the flowing channels in the flow–focusing region close to the orifice entrance. Similar to what occurs in Regime 2, the retardation effect not only deforms the fluid interface but only elevates the upstream pressure in the dispersed phase, which is shown in Figure 16. As the high pressure in the dispersed phase stabilizes the fluid interface, the squeezing rate is slowed down in this regime, which is evident from the slope of the corresponding neck evolution curve shown in Figure 14. However, the squeezing time interval required by the case with $Eu^{-1/2} = 4.765$ is less than that with $Eu^{-1/2} = 3.812$; consequently, the resultant droplet sizes with $Eu^{-1/2} = 4.765$ are smaller as well. Such differences are resulted from the formations of thin jets. Compared to that in the case with $Eu^{-1/2} = 3.812$, the maximum W_n^* of the jet is smaller; therefore, the amount of fluid that can be injected into the resultant droplet is confined by the small width of the jet. In addition, the reduced jet width requires less time to be squeezed to the critical neck width that the

surface tension force can snap off the jet from the dispersed phase. As evident in Figure 14, the

total squeezing time required by the case with $Eu^{-1/2} = 4.765$ is less than that with $Eu^{-1/2} = 3.812$.

Because of these two reasons, the droplets formed in this regime are smaller compared to those
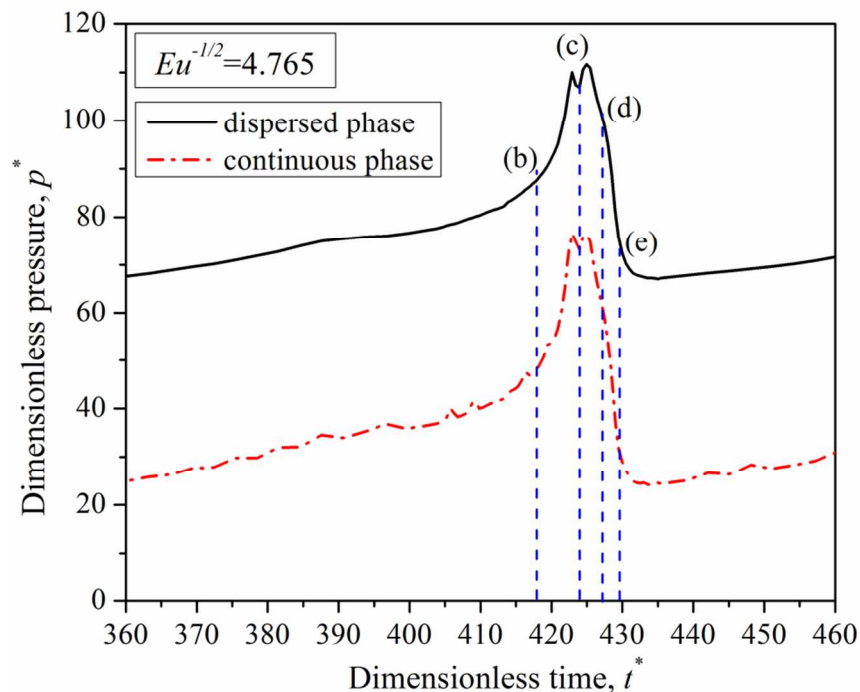
obtained in Regime 2.

Figure 16 Evolution of dimensionless upstream pressure, p^*, in the continuous and dispersed phases during the droplet breakup process with the operating conditions: $\mu_d/\mu_c = 50$, $Q_c/Q_d = 50$ and $Ca_c = 0.017$. The applied voltage V_0 is 480 V, corresponding to $Eu^{-1/2} = 4.765$. (b) ~ (e) correspond to the droplet breakup steps shown in Figure 15. The blue dot lines indicate the location of corresponding steps shown on the curves.

In Regime 2 and 3, the simulation results indicate that the squeezing effect contributed by

the continuous phase is vanished because of the overwhelmed pressure in the dispersed phase;

therefore, the advantages of the hydrodynamic flow–focusing over flow control do not exist in

these two regimes. We suggest applying relatively low voltages to microfluidic systems so that

the breakup processes are governed by Regime 1, where the advantages of the hydrodynamic

flow–focusing still preserve. Alternatively, one may alter the configurations of the applied

electric fields or the electric properties of the two phases that Taylor cones are not deformed by the electric fields.

4. Conclusion

In this study, we have adopted the conservative level–set method coupled with the perfect dielectric model to study the breakup process of viscous oil droplets inside an aqueous solution. When the viscosity in the dispersed phase is much higher than that in the continuous phase, the resultant droplets from a conventional microfluidic hydrodynamic flow–focusing device remain large sizes for a long range of operating flow ratios due to the viscous lubrication effect, indicating that the common operating approach which uses high flow ratios cannot increase the squeezing rate effectively during the squeezing stage of the droplet breakup process. In such circumstances, the active droplet–based microfluidics that incorporates the conventional microfluidic devices with external actuators, *i.e.*, external DC fields, has shown its unique ability in controlling the droplet breakup process. As a result of the different electric properties such as the permittivity and conductivity values between the two phases, the external electric field induces electric charges on the fluid interface. With appropriate configurations of the applied electric field, the electric force generated by the interactions of the electric field and electric charges exerts a squeezing effect on the fluid interface. If the electric force is decomposed along x and y coordinates, the component along the x direction clearly shows its role in squeezing the dispersed phase. As this component accelerates the squeezing rate, it consequently leads to droplets of reduced sizes. On the other hand, the component on the y direction is pointing opposite to the flow direction of the dispersed phase; therefore, it exerts a retardation effect to the dispersed phase.

With the assumption that both the continuous and dispersed phases can be regarded as dielectric fluids, the simulations in this study consider only the electric force induced by the

polarization charges. When the flow in the microfluidic device is in dripping regime and the applied voltage is increased from 0 V to 660 V, the droplet breakup process experiences three distinct regimes. In Regime 1 where the applied voltage is relatively low, corresponding to $Eu^{-1/2}$ between 0 and 2.38, the electric force assists the hydrodynamic forces to squeeze the dispersed phase, thus the obtained droplet sizes decrease linearly with the growth of the applied voltages. Because of the retardation effect resulted from the y component of the electric force, the upstream pressure in the dispersed phase increases accordingly with the growth of the applied voltages; meanwhile, the upstream pressure in the continuous phase is marginally influenced by the applied voltages. As a result, the squeezing effect contributed by the hydrodynamic forces is weakened by the increment of the applied voltages. In Regime 2 where $Eu^{-1/2}$ is in the range between 2.38 and 3.81, the squeezing effect is dominated by the electric force. The large retardation effect exerted by the electric force increases the pressure in the dispersed phase significantly for the entire breakup process. Such large pressure not only causes a considerable deformation of the dispersed phase in the flow–focusing region but also stabilizes the fluid interface during the squeezing stage. The competition between the squeezing and retardation effects prolongs the squeezing time; consequently, the resultant droplet sizes increase with the growth of the applied voltages in this regime. If the applied voltage is further increased to Regime 3 with $Eu^{-1/2}$ larger than 3.81, the dispersed phase deforms significantly and takes up most of the flowing channels in the flow–focusing region. Unsteady jets involve from the apex of the dispersed phase and are quickly pinched off because of their small widths. In this regime, the resultant droplet sizes decrease with the applied voltages again. As the advantages of hydrodynamic flow–focusing technique is undermined in Regime 2 and Regime 3, the microfluidic devices incorporated with external electric field are suggested to be operated with suitable applied voltages or with proper configurations of electric fields and properties of the two phases, which can limit the droplet breakup process in Regime 1 and prevents the deformation of the dispersed phase.

Appendix A Mesh Dependence Study

In order to eliminate the potential errors due to insufficient grid resolutions, a mesh dependence study was carried out with three types of meshes. These meshes have various numbers of elements across the width of orifice. For example, the corresponding numbers for Meshes 1, 2, 3 and 4 are 11, 14, 16 and 18, respectively, resulting in computational domains with different grid resolutions. The total numbers of computational cells in the domains are listed in Table A1. The operating conditions for the tested case were: $Q_c/Q_d = 50$, $\mu_d/\mu_c = 50$ and $Ca_c = 0.017$, respectively. As seen in Figure A1, the simulations using Mesh 1 generates numerical artefacts due to its low grid resolution. Bright dots appear inside the dispersed phase and around the generated droplets, which are due to the incorrect prediction of the level-set function ϕ. When the meshes of higher resolutions are used, these artefacts can be eliminated effectively. The corresponding droplet sizes predicted by these mesh resolutions are listed in Table A1. All these four meshes provide similar droplet sizes. As the number of elements increases, the relative errors of the predicted droplet sizes decrease slightly. Comparing the dimensionless droplet size in Mesh 3 with that in Mesh 4, the relative errors is negligible. In order to save our simulation time, we adopted Mesh 3 for the numerical investigations in this study.

Table A1 Results of mesh dependence study

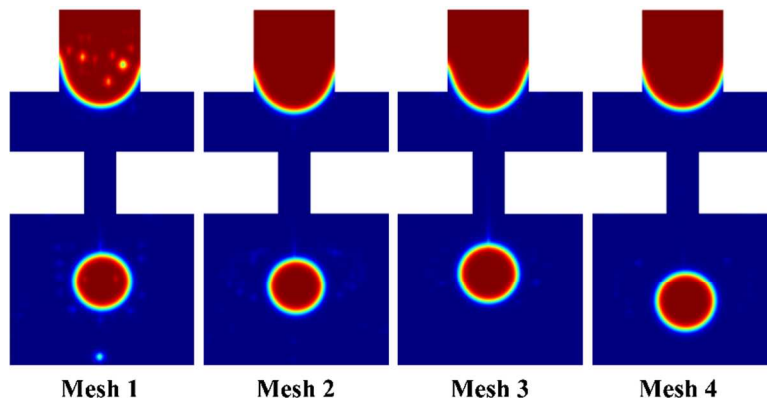| Mesh Type	1	2	3	4
Number of nodes across the orifice	11	14	16	23
Number of elements in total	5,349	8,794	13,160	31,740
Dimensionless droplet sizes	1.736	1.748	1.770	1.772

Figure A1 Contours of the predicted volume fraction by using three types of grid resolutions. The corresponding operating conditions are $\mu_d/\mu_c = 50$, $Q_c/Q_d = 50$ and $Ca_c = 0.017$.

Appendix B Simulation setup for the droplet deformation problem

Although the accuracy of LSM in predicting the droplet breakup process governed by hydrodynamics has been validated, it is still necessary to validate the accuracy of our numerical model in predicting the droplet breakup process controlled by electric field. Currently we lack of direct experimental evidence to compare with. Therefore, we applied the numerical model that couples LSM with electrostatic model to study the classic droplet deformation problem, which can validate the numerical model alternatively. There are several discussions regarding this problem in literatures[29, 31, 44].

The geometry used in the simulations is shown in Figure B(a). The simulations were carried out in a two-dimensional axisymmetric (2D-axisymmetric) computational domain, which adopted the triangular unstructured mesh. The regions where the deformed droplet might propagate were refined with very fine mesh resolutions. The number of elements in this problem is approximately 40,000. The parameters used by the simulations are listed in Table B1.The governing equations and parameters were normalized using the scales similar to those shown in Section 2. The time was scaled by the characteristic time scale for oscillation of an inviscid

37

droplet[31, 41], which is expressed as $\tau = \sqrt{\frac{1}{24}(2\rho_c + 3\rho_d)R_0^3/\sigma}$. The simulation reached steady

state when the dimensionless time t^* exceeded 60. The relevant results are provided in Figure 7.
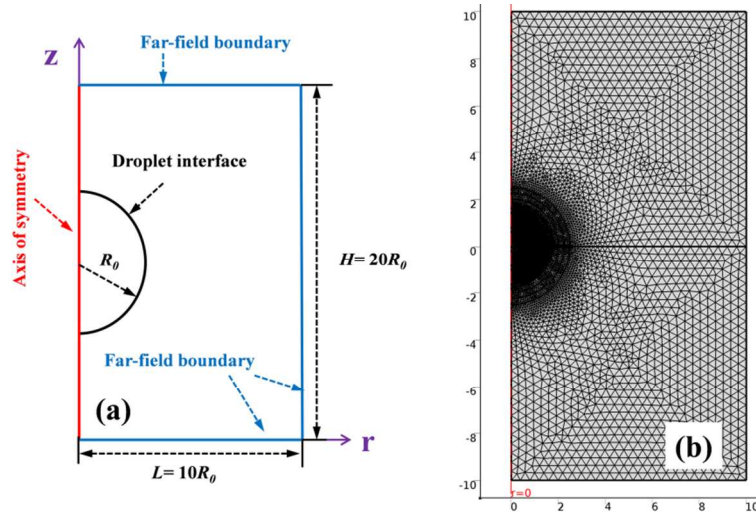

Figure B1 (a) 2D-axisymmetric geometry for the numerical simulation. (b) A typical mesh used by the simulation.

Table B1 Simulation parameters for the droplet deformation problem
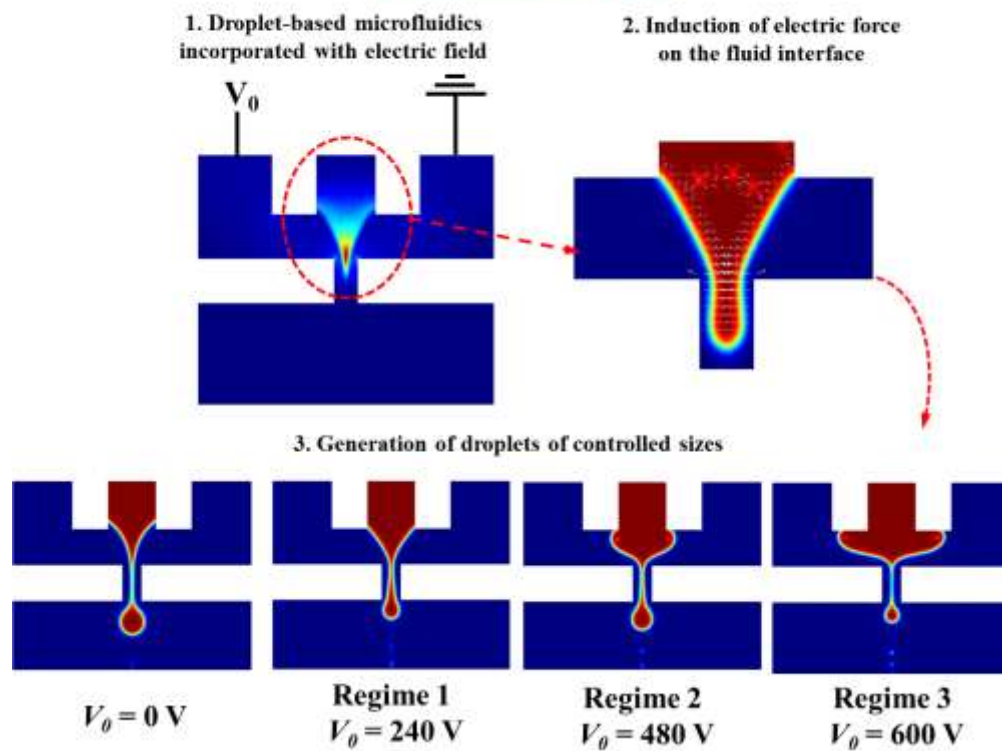
Applied Electric field, E_0	1.5×10^5 V/m
Radius of the droplet, R_0	1×10^{-3} m
Permittivity of the droplet, ε_d	$10 \times 8.854 \times 10^{-12}$ C/(V*m)
Permittivity of the suspending medium, ε_c	8.854×10^{-12} C/(V*m)
Interfacial tension, σ	3.2×10^{-3} N/m
Density of the droplet, ρ_d	1000 kg/m³
Density of the suspending medium, ρ_c	1000 kg/m³
Viscosity of the droplet, μ_d	1×10^{-3} Pa*s
Viscosity of the suspending medium, μ_c	1×10^{-3} Pa*s

References

1. A. Gunther and K. F. Jensen, *Lab on a Chip*, 2006, **6**, 1487-1503.
2. S. Marre and K. F. Jensen, *Chem. Soc. Rev.*, 2010, **39**, 1183-1202.
3. H. Song, D. L. Chen and R. F. Ismagilov, *Angew. Chem.-Int. Edit.*, 2006, **45**, 7336-7356.
4. J. D. Tice, H. Song, A. D. Lyon and R. F. Ismagilov, *Langmuir*, 2003, **19**, 9127-9133.
5. K. P. Nichols, R. R. Pompano, L. Li, A. V. Gelis and R. F. Ismagilov, *J. Am. Chem. Soc.*, 2011, **133**, 15721-15729.
6. Y. H. Li, R. K. Reddy, C. S. S. R. Kumar and K. Nandakumar, *Biomicrofluidics*, 2014, **8**.
7. Y. J. Song, J. Hormes and C. Kumar, *Small*, 2008, **4**, 698-711.

8. K. S. Krishna, Y. H. Li, S. N. Li and C. S. S. R. Kumar, *Adv Drug Deliver Rev*, 2013, **65**, 1470-1495.
9. L. Y. Yeo, H. C. Chang, P. P. Y. Chan and J. R. Friend, *Small*, 2011, **7**, 12-48.
10. G. F. Christopher and S. L. Anna, *J. Phys. D-Appl. Phys.*, 2007, **40**, R319-R336.
11. P. Garstecki, M. J. Fuerstman, H. A. Stone and G. M. Whitesides, *Lab on a Chip*, 2006, **6**, 437-446.
12. S. L. Anna, N. Bontoux and H. A. Stone, *Applied Physics Letters*, 2003, **82**, 364-366.
13. Z. H. Nie, M. S. Seo, S. Q. Xu, P. C. Lewis, M. Mok, E. Kumacheva, G. M. Whitesides, P. Garstecki and H. A. Stone, *Microfluid. Nanofluid.*, 2008, **5**, 585-594.
14. H. Willaime, V. Barbier, L. Kloul, S. Maine and P. Tabeling, *Phys. Rev. Lett.*, 2006, **96**.
15. S. K. Hsiung, C. T. Chen and G. B. Lee, *J. Micromech. Microeng.*, 2006, **16**, 2403-2410.
16. T. Franke, A. R. Abate, D. A. Weitz and A. Wixforth, *Lab on a Chip*, 2009, **9**, 2625-2627.
17. Z. C. Wang and J. A. Zhe, *Lab on a Chip*, 2011, **11**, 1280-1285.
18. O. Ozen, N. Aubry, D. T. Papageorgiou and P. G. Petropoulos, *Phys. Rev. Lett.*, 2006, **96**.
19. D. R. Link, E. Grasland-Mongrain, A. Duri, F. Sarrazin, Z. D. Cheng, G. Cristobal, M. Marquez and D. A. Weitz, *Angew. Chem.-Int. Edit.*, 2006, **45**, 2556-2560.
20. D. A. Sessoms, M. Belloul, W. Engl, M. Roche, L. Courbin and P. Panizza, *Physical Review E*, 2009, **80**, 016317.
21. M. Belloul, J. F. Bartolo, B. Ziraoui, F. Coldren, V. Taly and A. I. El Abed, *Applied Physics Letters*, 2013, **103**.
22. L. Ding, T. Lee and C. H. Wang, *J. Controlled Release*, 2005, **102**, 395-413.
23. J. W. Xie, J. C. M. Marijnissen and C. H. Wang, *Biomaterials*, 2006, **27**, 3321-3332.
24. H. Kim, D. W. Luo, D. Link, D. A. Weitz, M. Marquez and Z. D. Cheng, *Applied Physics Letters*, 2007, **91**.
25. S. Osher and J. A. Sethian, *J. Comput. Phys.*, 1988, **79**, 12-49.
26. M. Sussman, P. Smereka and S. Osher, *J. Comput. Phys.*, 1994, **114**, 146-159.
27. E. Olsson and G. Kreiss, *J. Comput. Phys.*, 2005, **210**, 225-246.
28. D. A. Saville, *Annu. Rev. Fluid Mech.*, 1997, **29**, 27-64.
29. E. K. Zholkovskij, J. H. Masilyah and J. Czarnecki, *J. Fluid Mech.*, 2002, **472**, 1-27.
30. J. H. Masliyah and S. Bhattacharjee, *Electrokinetic and colloid transport phenomena*, Wiley-Interscience, Hoboken, N.J., 2006.
31. G. Supeene, C. R. Koch and S. Bhattacharjee, *J. Colloid Interface Sci.*, 2008, **318**, 463-476.
32. C. Pantano, A. M. Ganan-Calvo and A. Barrero, *J. Aerosol Sci*, 1994, **25**, 1065-1077.
33. A. M. Ganan-Calvo, *J. Fluid Mech.*, 1997, **335**, 165-188.
34. N. K. Nayyar and G. S. Murty, *P Phys Soc Lond*, 1960, **75**, 369-373.
35. J. R. Melcher and G. I. Taylor, *Annu. Rev. Fluid Mech.*, 1969, **1**, 111-&.
36. J. D. Wehking, L. Chew and R. Kumar, *Applied Physics Letters*, 2013, **103**.
37. S. Bashir, J. M. Rees and W. B. Zimmerman, *Chem Eng Sci*, 2011, **66**, 4733-4741.
38. M. De Menech, P. Garstecki, F. Jousse and H. A. Stone, *J. Fluid Mech.*, 2008, **595**, 141-161.
39. O. Reynolds, *Phil. Trans. R. Soc. Lond*, 1886, **177**, 157-234.
40. C. T. Okonski and H. C. Thacher, *J. Phys. Chem.*, 1954, **57**, 955-958.
41. D. L. Whitaker, C. Kim, C. L. Vicente, M. A. Weilert, H. J. Maris and G. M. Seidel, *J. Low Temp. Phys.*, 1998, **113**, 491-499.
42. C. H. Yeh, M. H. Lee and Y. C. Lin, *Microfluid. Nanofluid.*, 2012, **12**, 475-484.
43. H. B. Zhang, M. J. Edirisinghe and S. N. Jayasinghe, *J. Fluid Mech.*, 2006, **558**, 103-111.
44. H. Sato, N. Kaji, T. Mochizuki and Y. H. Mori, *Phys. Fluids*, 2006, **18**.

40

Using external electric field to control the breakup of viscous droplets inside a microfluidic device

1. Droplet-based microfluidics incorporated with electric field

V_0

2. Induction of electric force on the fluid interface

3. Generation of droplets of controlled sizes

$V_0 = 0$ V

Regime 1
$V_0 = 240$ V

Regime 2
$V_0 = 480$ V

Regime 3
$V_0 = 600$ V

330x285mm (96 x 96 DPI)